Commun. Comput. Phys.
doi: 10.4208/cicp.OA-2017-0039

Vol. **22**, No. 5, pp. 1385-1412
November 2017

A Novel Multi-Dimensional Limiter for High-Order Finite Volume Methods on Unstructured Grids

Yilang Liu[1], Weiwei Zhang[1,*] and Chunna Li[2]

[1] *School of Aeronautics, Northwestern Polytechnical University, No. 127 Youyi West Road, Xi'an 710072, China.*
[2] *National Key Laboratory of Aerospace Flight Dynamics, School of Astronautics, Northwestern Polytechnical University, No. 127 Youyi West Road, Xi'an 710072, China.*

Communicated by Chi-Wang Shu

Received 21 February 2017; Accepted (in revised version) 17 April 2017

Abstract. This paper proposes a novel distance derivative weighted ENO (DDWENO) limiter based on fixed reconstruction stencil and applies it to the second- and high-order finite volume method on unstructured grids. We choose the standard deviation coefficients of the flow variables as the smooth indicators by using the k-exact reconstruction method, and obtain the limited derivatives of the flow variables by weighting all derivatives of each cell according to smoothness. Furthermore, an additional weighting coefficient related to distance is introduced to emphasize the contribution of the central cell in smooth regions. The developed limiter, combining the advantages of the slope limiters and WENO-type limiters, can achieve the similar effect of WENO schemes in the fixed stencil with high computational efficiency. The numerical cases demonstrate that the DDWENO limiter can preserve the numerical accuracy in smooth regions, and capture the shock waves clearly and steeply as well.

AMS subject classifications: 35L25, 65M08, 65M12, 74J40

Key words: High-order finite volume method, unstructured grids, DDWENO limiter, shock waves.

1 Introduction

Computational fluid dynamics (CFD) researchers have kept pursuing the accuracy of numerical simulation and its adaptability to complex configurations. Although the second-order accuracy schemes have played an important role in aircraft design and application [1–4], they still have large numerical dissipation and dispersion. For some complex

*Corresponding author. *Email addresses:* aeroelastic@nwpu.edu.cn (W. W. Zhang), liuyilang1212112@163.com (Y. L. Liu), chunnali@nwpu.edu.cn (C. N. Li)

 ©2017 Global-Science Press

https://doi.org/10.4208/cicp.OA-2017-0039 Published online by Cambridge University Press

flow problems, such as wave propagation, vortex-dominated flows including high-lift configuration, helicopter blade vortex interaction, as well as large eddy simulation and direct numerical simulation of turbulence, high-order accuracy schemes must be used to obtain more elaborate and detailed results [5]. However, whether for the second- or the high-order scheme, an outstanding issue of solving discontinuous flowfields is how to clearly and precisely capture shock waves and suppress non-physical oscillations near discontinuities. It is technically difficult to develop higher-order schemes on unstructured grids, as they tend to have lower dissipation and weaker robustness compared with second-order schemes [6, 7]. Therefore, an efficient and accurate oscillation control strategy should be incorporated into both the second- and the high-order numerical schemes.

Limiting the numerical process is one of the most commonly used ways to deal with discontinuities, such as shock waves. Currently, there are mainly three types of limiters. The first one is using artificial viscosity [8–10]. This limiter can smooth numerical oscillations near shock waves by introducing artificial dissipative terms into flow control equations. It is robust and easy to implement. However, the value of the additional terms needs to be modulated by free parameters. Besides, the artificial viscosity is a kind of numerical viscosity, which may affect the real physical viscosity to a certain extent, especially for viscous flows.

The second limiter utilizes ENO/WENO schemes [11–24]. The ENO schemes, first proposed by Harten [11, 12], have been successfully applied in flowfield with strong shock waves. The smoothest stencil is selected to reconstruct the distribution of flow variables; while other stencils containing discontinuities are all discarded. Unlike ENO, the WENO schemes [13–17] combine all of the stencils by assigning a nonlinear weight coefficient to each reconstruction stencil based on the local smoothness of flowfield. Although the WENO schemes show superior advantages in capturing shocks and have been successfully applied, it is a enormous task to choose admissible and proper stencils from a large number of cells, especially for high-order and multi-dimensional cases on unstructured grids. Qiu and Shu [18] proposed the Hermite WENO (HWENO) scheme and used it as a limiter for Runge-Kutta discontinuous Galerkin method. In comparison with traditional WENO schemes, the main difference of the HWENO scheme is that both the function and its first derivatives are evolved in time and used in reconstruction. Therefore, the scheme has a more compact stencil for the same order of accuracy, and it is widely used on unstructured grids to control spurious oscillations, especially for discontinuous Galerkin method [19]. However, both the flow variables and their derivatives of each cell are evolved in time marching, and more storage and CPU time are required. Rather than choosing candidate stencils, Ivan and Groth [20] proposed a high-order central ENO (CENO) finite volume scheme for solving compressible flows on unstructured grids. The method is performed on fixed central stencils, which involves an unlimited k-exact reconstruction in smooth regions, and switches a limited piecewise linear reconstruction when discontinuities are identified. The CENO scheme is also extended to three-dimensional cases, in which the robustness and the high-order accuracy

https://doi.org/10.4208/cicp.OA-2017-0039 Published online by Cambridge University Press

are validated by numerical results [21–24].

The third one is the slope limiter [25–41]. Barth and Jespersen [25] designed a slope limiter according to the maximum principle on unstructured grids for the first time. This limiter can effectively suppress numerical oscillation near shock waves. However, they also introduce the non-differentiable limited function, which will destroy the convergence properties of the flow solver. For this reason, Venkatakrishnan [26] improved Barth's limiter by replacing the limited function with a smooth, differentiable one. The improved limiter shows the better convergence for discontinuous flowfield, and has been widely used [27,28]. Accordingly, other researchers proposed multi-dimensional limiting process (MLP) [29, 30] strategies, and have successfully extended them to unstructured grids. Those strategies are quite effective in controlling multi-dimensional oscillations, as well as accurately capturing flow features [31–33]. Jawahar and Kamath [34] developed a Van Albada-typed limiting procedure and used it in the second-order finite volume method on unstructured grids. The limiter is differentiable, and shows excellent performance in controlling oscillations without reducing the accuracy of the smooth extreme regions. Hence it has been widely used in finite volume method and discontinuous Galerkin method (DG) [35–37]. Choi and Liu [38] have firstly proposed a biased averaging procedure (BAP), and applied it to solve Euler equations on structured grids. The BAP limiter transforms the gradients of the flow variables contained in the stencil with biased average function, and then reduces the real gradients of the flow variables by inverse transformation with the self-similar function. This limiter is simple to be implemented and parameter-free, and it is also differentiable and efficient to be extended to unstructured grids. Li and Ren [39, 40] extended the BAP limiter to a high-order finite volume scheme on unstructured grids based on secondary reconstruction (SR), termed weighted BAP (WBAP) limiter. The mechanism for controlling the numerical oscillations is also illustrated in their paper, and the WBAP limiter is robust and accurate in capturing shock waves and contact discontinuities. Liu [41] also developed a distance weighted BAP (DWBAP) limiter and applied it on unstructured grids for the two- and three-dimensional cases, which also achieved a good effect.

A great challenge to limiters designed for high-order schemes is to preserve numerical accuracy in smooth regions, and be robust and effective in coping with discontinuities, such as shock waves. The ENO/WENO schemes are able to handle discontinuities, and can preserve numerical accuracy. However, both the ENO and WENO schemes encounter difficulties in selecting appropriate stencils on general multi-dimensional unstructured grids, which requires much more memory and computational cost. The CENO method avoids the complexity of selecting multiple stencils, since it implements the unlimited high-order k-exact reconstruction in smooth regions and switches to limiting with respect to smooth indicator by Barth's limiter in discontinuities. But in essence it can still be considered as a kind of slope limiters. In comparison with the ENO/WENO schemes, the slope limiter usually limits the gradients of flow variables that are difficult to be considered in both numerical accuracy and computational convergence.

This paper combines the WENO scheme with the slope limiter, and develops a novel

https://doi.org/10.4208/cicp.OA-2017-0039 Published online by Cambridge University Press

distance derivative weighted ENO (DDWENO) limiter, which is suitable for both the second- and high-order finite volume methods. Unlike WENO scheme, we evaluate the smoothness of each cell in the initial k-exact reconstruction steps based on the fixed stencil. Further in the limiting steps, all the derivatives of the flow variables for each cell are weighted according to the smoothness indicator for the same reconstruction stencil. Meanwhile, nonlinear weighting coefficients related to distance are also introduced to ensure the numerical accuracy in smooth regions. The developed DDWENO limiter has high computational efficiency because it avoids the complexity in choosing candidate stencils. It can capture shock waves sharply and has a good property of convergence for discontinuous flows.

The outline of this paper is as follows. Section 2 describes the high-order finite volume method and the k-exact reconstruction briefly. The DDWENO limiting procedure for the second- and high-order finite volume schemes is introduced in detail in Section 3. Section 4 presents several numerical examples to assess the performance of the limiter, and conclusions are drawn in Section 5.

2 Governing equations and the finite volume method

2.1 The high-order finite volume method on unstructured grids

The integral form of two-dimensional Euler equations can be written as:

$$\frac{\partial}{\partial t}\int_{\Omega} \boldsymbol{Q} d\Omega + \oint_{\partial\Omega} \boldsymbol{F}(\boldsymbol{Q})\cdot \boldsymbol{n} d\Gamma = 0, \tag{2.1}$$

where Ω is the control volume; $\partial\Omega$ is the boundary of control volume; and $\boldsymbol{n}=(n_x,n_y)^T$ denotes the unit outward normal vector to the boundary. The vector of the conservative variables $\boldsymbol{Q}$ and the column vectors of the inviscid flux matrix $\boldsymbol{F}(\boldsymbol{Q})=(\boldsymbol{F}_x(\boldsymbol{Q}),\boldsymbol{F}_y(\boldsymbol{Q}))$ are given as follows:

$$\boldsymbol{Q}=\begin{bmatrix}\rho\\ \rho u\\ \rho v\\ E\end{bmatrix},\quad \boldsymbol{F}_x(\boldsymbol{Q})=\begin{bmatrix}\rho u\\ \rho u^2+p\\ \rho uv\\ u(E+p)\end{bmatrix},\quad \boldsymbol{F}_y(\boldsymbol{Q})=\begin{bmatrix}\rho v\\ \rho uv\\ \rho v^2+p\\ v(E+p)\end{bmatrix},$$

where ρ denotes the density; u and v are the y direction components of the velocity vector; p is the pressure and E is the total energy per unite volume. The equation of state for the ideal gas is

$$p=(\gamma-1)\left[E-\frac{\rho}{2}(u^2+v^2)\right], \tag{2.2}$$

where γ is the ratio of specific heats, and for the ideal gas γ is equal to 1.4.

In the cell-centered finite volume method, the computational domain is divided into non-overlapping control volumes that completely cover the domain. Interface variables

https://doi.org/10.4208/cicp.OA-2017-0039 Published online by Cambridge University Press

are derived from average values of the cells to calculate fluxes of the control volumes. Through the spatial discretization, the integral equations are translated into ordinary differential equations in time, and the flow variables are computed by the time marching method. The semi-discrete finite volume formulation of the flow equations is

$$\frac{d\overline{\boldsymbol{Q}}_i}{dt}=-\frac{1}{|\boldsymbol{\Omega}_i|}\sum_{m=1}^{N(i)}\sum_{q=1}^{N_q}|\Gamma_{i,m}|\omega_q\boldsymbol{F}(\boldsymbol{Q}(x_q,y_q))\cdot\boldsymbol{n}_{i,m}, \tag{2.3}$$

where $|\Omega_i|$ denotes the volume for the ith cell; $N(i)$ is the set of cells neighboring the cell i; and $|\Gamma_{i,m}|$ is the interface area between the cell i and the neighbor cell m. (x_q,y_q) denotes the Gauss quadrature point with quadrature weight ω_q, and N_q is the sum of Gauss points on the interface; and $\boldsymbol{n}_{i,m}$ is the outer normal vector of the interface between cell i and m. The average conservative vector of the control volume i is $\overline{\boldsymbol{Q}}_i$, which is computed by

$$\overline{\boldsymbol{Q}}_i=\frac{1}{|\boldsymbol{\Omega}_i|}\int_{\Omega_i}\boldsymbol{Q}(x,y)d\Omega. \tag{2.4}$$

The numerical fluxes at the right hand of Eq. (2.3) can be evaluated by upwind schemes. According to the Godunov-type method, the interface normal fluxes are calculated by the Riemann solver:

$$\boldsymbol{F}(\boldsymbol{Q}_{i,m})\cdot\boldsymbol{n}_{i,m}\approx\widetilde{\boldsymbol{F}}(\boldsymbol{Q}_{i,m}^L,\boldsymbol{Q}_{i,m}^R,\boldsymbol{n}_{i,m}), \tag{2.5}$$

where the superscript "L" and "R" denote the states of the flow variables approaching to the left and right sides of the cell interface, respectively. This paper adopts the Roe [42] scheme to compute numerical fluxes, where $\boldsymbol{Q}_{i,m}^L$ and $\boldsymbol{Q}_{i,m}^R$ are used to evaluate Roe's average states. The middle point of each interface is used to calculate the fluxes in the second-order accuracy method, and two Gauss points are used in the third- and fourth-order method. According to Gauss integral theory, the numerical order can achieve $2N+1$ when using $N+1$ integral points. Therefore, two Gauss points can accurately compute the integral of cubic polynomials on the cell interface for the fourth-order scheme.

The semi-discrete formulation of Eq. (2.3) can be translated into ordinary differential equations in time after obtaining the discrete numerical fluxes:

$$\frac{d\overline{\boldsymbol{Q}}_i}{dt}=\overline{\boldsymbol{R}}_i, \tag{2.6}$$

where $\overline{\boldsymbol{R}}_i$ denotes the sum of inviscid fluxes. Finally, the semi-discrete system of Eq. (2.6)

https://doi.org/10.4208/cicp.OA-2017-0039 Published online by Cambridge University Press

is marched in time using an explicit four-stage Runge-Kutta scheme [43]:

$$\begin{aligned}
&\overline{\boldsymbol{Q}}_i^{(0)} = \overline{\boldsymbol{Q}}_i^{t},\\
&\overline{\boldsymbol{Q}}_i^{(1)} = \overline{\boldsymbol{Q}}_i^{(0)} + \alpha_1 \Delta t \overline{\boldsymbol{R}}_i^{0},\\
&\overline{\boldsymbol{Q}}_i^{(2)} = \overline{\boldsymbol{Q}}_i^{(0)} + \alpha_2 \Delta t \overline{\boldsymbol{R}}_i^{1},\\
&\overline{\boldsymbol{Q}}_i^{(3)} = \overline{\boldsymbol{Q}}_i^{(0)} + \alpha_3 \Delta t \overline{\boldsymbol{R}}_i^{2},\\
&\overline{\boldsymbol{Q}}_i^{(4)} = \overline{\boldsymbol{Q}}_i^{(0)} + \alpha_4 \Delta t \overline{\boldsymbol{R}}_i^{3},\\
&\overline{\boldsymbol{Q}}_i^{(t+1)} = \overline{\boldsymbol{Q}}_i^{4},
\end{aligned} \tag{2.7}$$

where the constant values are set as $\alpha_1 = \frac{1}{4}$, $\alpha_2 = \frac{1}{3}$, $\alpha_3 = \frac{1}{2}$, $\alpha_4 = 1$. For steady problems, local time steps can be employed to accelerate convergence.

2.2 High-order k-exact solution reconstruction

The key issue to solve flow equations by the finite volume method is to reconstruct the distributions of unknown variables at the interface of control volumes using cell average state variables, which is directly related to the accuracy of the numerical solution. In this paper, the k-exact least-squares method is adopted to conduct accurate high-order reconstruction. For brevity, we will describe the process of flowfield reconstruction in two-dimension.

For a component of the conservative variables denoted by $Q(x,y)$, which satisfies the conservation of the mean property in the following equations

$$\overline{Q}_i = \frac{1}{\Omega_i}\int_{\Omega_i} Q(x,y)d\Omega, \tag{2.8}$$

where $\overline{Q}_i$ is the mean value of the control volume i. The Taylor series expansion of $Q(x,y)$ at the centroid of a cell can be written as

$$\begin{aligned}
Q(x,y) =& Q_i + \frac{\partial Q}{\partial x}|_{r_i}(x-x_i) + \frac{\partial Q}{\partial y}|_{r_i}(y-y_i) + \frac{1}{2}\frac{\partial^2 Q}{\partial x^2}|_{r_i}(x-x_i)^2\\
&+ \frac{\partial^2 Q}{\partial x \partial y}|_{r_i}(x-x_i)(y-y_i) + \frac{1}{2}\frac{\partial^2 Q}{\partial y^2}|_{r_i}(y-y_i)^2 + \mathcal{O}(h^3).
\end{aligned} \tag{2.9}$$

Substitute the above expansion into Eq. (2.8), and we will obtain:

$$\overline{Q}_i = Q_i + \frac{\partial Q}{\partial x}|_{r_i}\cdot\overline{x}_i + \frac{\partial Q}{\partial y}|_{r_i}\cdot\overline{y}_i + \frac{1}{2}\frac{\partial^2 Q}{\partial x^2}|_{r_i}\cdot\overline{x^2}_i + \frac{\partial^2 Q}{\partial x \partial y}|_{r_i}\cdot\overline{xy}_i + \frac{1}{2}\frac{\partial^2 Q}{\partial y^2}|_{r_i}\cdot\overline{y^2}_i + \mathcal{O}(h^3), \tag{2.10}$$

where $\overline{x^a y^a}$ is called zero-mean basis, and it is defined as:

$$\overline{x^a y^a} = \frac{1}{\Omega_i}\int_{\Omega_i}(x-x_i)^a(y-y_i)^b d\Omega.$$

https://doi.org/10.4208/cicp.OA-2017-0039 Published online by Cambridge University Press

We substitute the Eq. (2.10) into Eq. (2.9) and replace the variable Q_i, thus we obtain

$$\begin{aligned} Q(x,y) =& \overline{Q}_i + \frac{\partial Q}{\partial x}|_{r_i}[(x-x_i)-\overline{x}_i] + \frac{\partial Q}{\partial y}|_{r_i}[(y-y_i)-\overline{y}_i] + \frac{1}{2}\frac{\partial^2 Q}{\partial x^2}|_{r_i}[(x-x_i)^2-\overline{x^2}_i \\ &+ \frac{\partial^2 Q}{\partial x \partial y}|_{r_i}[(x-x_i)(y-y_i)-\overline{xy}_i] + \frac{1}{2}\frac{\partial^2 Q}{\partial y^2}|_{r_i}[(y-y_i)^2-\overline{y^2}_i] + \mathcal{O}(h^3). \end{aligned} \tag{2.11}$$

For a reconstruction stencil $S_i = \{V_1, V_2, \cdots, V_i, V_n\}$, where V_i stands for the ith control volume, as is shown in Fig. 1, we apply Eq. (2.10) to each control volume within the stencil. Thus a system of linear algebraic equations can be obtained:

$$A \cdot B = C, \tag{2.12}$$

where

$$A = \begin{bmatrix} \Delta x_{1i}-\overline{x}_{1i} & \Delta y_{1i}-\overline{y}_{1i} & \Delta x_{1i}^2-\overline{x^2}_{1i} & (\Delta x\Delta y)_{1i}-\overline{xy}_{1i} & \Delta y_{1i}^2-\overline{y^2}_{1i} & \cdots \\ \Delta x_{2i}-\overline{x}_{2i} & \Delta y_{2i}-\overline{y}_{2i} & \Delta x_{2i}^2-\overline{x^2}_{2i} & (\Delta x\Delta y)_{2i}-\overline{xy}_{2i} & \Delta y_{2i}^2-\overline{y^2}_{2i} & \cdots \\ \Delta x_{3i}-\overline{x}_{3i} & \Delta y_{3i}-\overline{y}_{3i} & \Delta x_{3i}^2-\overline{x^2}_{3i} & (\Delta x\Delta y)_{3i}-\overline{xy}_{3i} & \Delta y_{3i}^2-\overline{y^2}_{3i} & \cdots \\ \cdots & \cdots & \cdots & \cdots & \cdots & \ddots \\ \Delta x_{ni}-\overline{x}_{ni} & \Delta y_{ni}-\overline{y}_{ni} & \Delta x_{ni}^2-\overline{x^2}_{ni} & (\Delta x\Delta y)_{ni}-\overline{xy}_{ni} & \Delta y_{ni}^2-\overline{y^2}_{ni} & \cdots \end{bmatrix},$$

$$B = \begin{bmatrix} \frac{\partial Q}{\partial x}|_{r_i} \\ \frac{\partial Q}{\partial y}|_{r_i} \\ \frac{1}{2}\frac{\partial^2 Q}{\partial x^2}|_{r_i} \\ \frac{\partial^2 Q}{\partial x \partial y}|_{r_i} \\ \frac{1}{2}\frac{\partial^2 Q}{\partial y^2}|_{r_i} \end{bmatrix} \begin{bmatrix} \overline{Q}_1-\overline{Q}_i \\ \overline{Q}_2-\overline{Q}_i \\ \overline{Q}_3-\overline{Q}_i \\ \vdots \\ \overline{Q}_n-\overline{Q}_i \end{bmatrix}, \qquad (\Delta x^a \Delta y^a)_{ni} = (x_n-x_i)^a (y_n-y_i)^b.$$

Generally, the number of the control volumes in the stencil should be more than the number of derivatives to be computed. Thus Eq. (2.12) is an over-determined system, which can be solved by a least-squares method. After solving Eq. (2.12), all the derivatives of $Q(x,y)$ can be obtained. Considering that the matrix "A" in Eq. (2.12) is only related to the geometric property of the control volume, we can compute and prestore the general inverse matrix of "A" based on the singular value decomposition method. Therefore, the least-squares problem can be replaced by a matrix-vector multiplication in pseudo-time iterations, significantly reducing the computational time but requiring more memory.

https://doi.org/10.4208/cicp.OA-2017-0039 Published online by Cambridge University Press

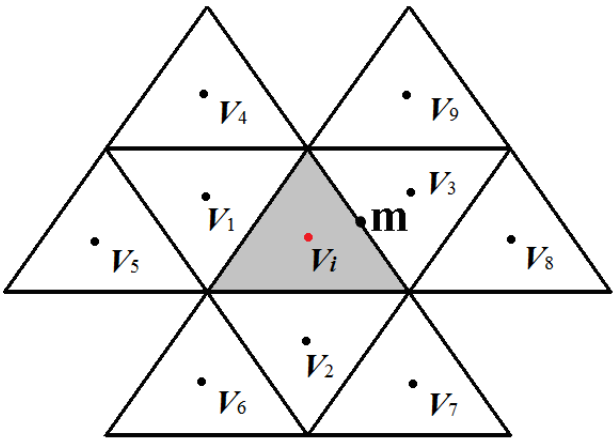


Figure 1: Reconstruction stencil.

3 Design of the DDWENO limiter

In this section, we mainly expatiate the designing of the DDWENO limiter based on high-order k-exact reconstruction. All the derivatives of flow variables can be obtained by the k-exact reconstruction method mentioned in Section 2.2. These initial derivatives are calculated based on fixed stencils, which are accurate only if the distributions of flow variables for the stencils are smooth enough. However, for flows with discontinuities, the monotonic limiting strategy is required for eliminating non-physical oscillations in discontinuous regions caused by high-order interpolations. The process of the developed DDWENO limiter can be divided into two steps. The first step is to implement initial k-exact reconstruction in the fixed stencil, and meanwhile to compute the smoothness indicator of each stencil, which is considered as the smoothness of the central cell. In the second step, all the derivatives in the same fixed stencil are limited and weighted according to the smoothness of each cell. The complexity of choosing multiple candidate stencils is ingeniously avoiding, since both steps are accomplished based on the fixed stencil. Further, the conception of the WENO scheme is incorporated into the developed DDWENO limiter, and hence the spurious oscillations can be efficiently suppressed with a good property of convergence.

3.1 Smoothness indicator based on the standard deviation coefficients

The smoothness indicator can measure smoothness of flow variables for a stencil. In this section, a new smooth indicator is presented. We compute the standard deviation coefficients of pressure for each stencil to represent the smoothness. It is very simple and easy to implement, since only cell averaged values in the stencil are needed. The standard deviation coefficients can accurately detect shock discontinuities and have high efficiency, especially on unstructured grids. The standard deviation coefficients χ are

https://doi.org/10.4208/cicp.OA-2017-0039 Published online by Cambridge University Press

defined as the ratio of the standard deviation σ to the average value $\overline{X}$ of the stencil, and the range span of χ is $\chi>0$

$$\chi=\frac{\sigma}{\overline{X}},\quad \sigma=\sqrt{\frac{1}{n}\sum_{i=1}^{n}(X_i-\overline{X})^2}, \tag{3.1}$$

where n is the number of cells in a reconstruction stencil. The value of the standard deviation coefficients stand for the smoothness of a stencil. In smooth regions, the coefficients are very small, approaching to zero. But in discontinuous regions, it is relatively large.

In initial k-exact reconstruction step, we need to compute and store the standard deviation coefficients χ for the central cell in the fixed stencil. In the limiting step, the coefficients χ are used as the smoothness indicator. Therefore, all the derivatives of each cell can be weighted according to the value of χ.

3.2 The process of the DDWENO limiter

The main conception of the DDWENO limiter is to weight all the derivatives of flow variables of each cell in the fixed reconstruction stencil according to the smoothness indicator. Therefore, the derivatives of the central cell can be efficiently reconstructed and limited to suppress non-physical oscillations. Let $\widetilde{g_{central}}$ denote the limited components of the derivatives of the central cell in the stencil and $L(g)$ the limiting function:

$$\widetilde{g_{central}}=L(g_1,g_2,\cdots,g_n), \tag{3.2}$$

where g denotes the components of the initial derivatives of flow variables obtained by initial unlimited k-exact reconstruction in the fixed stencil.

Firstly, the derivatives in the stencil are weighted according to the smoothness indicators of each cell. Considering that the larger the standard deviation coefficient is, the stronger discontinuity the cell approaches, hence, we weight the derivatives by the inverse of the standard deviation coefficients, and the weighted coefficients of each cell $\omega_i^{(1)}$ can be expressed as follows

$$\omega_i^{(1)}=\frac{\alpha_i}{\sum_{i=1}^{n}\alpha_i},\quad \alpha_i=\frac{1}{\chi_i+\delta},\quad (i=1,2,\cdots,n), \tag{3.3}$$

where δ is a tolerance to avoid being divided by zero, which can be set as 10^{-8}. χ_i denotes the standard deviation coefficients of cell i, which are computed by the fixed stencil centered at cell i in the initial k-exact reconstruction step. $\omega_i^{(1)}$ is the nonlinear weighting coefficient related to flow variables. For the cell with large derivatives, the values of the weighting coefficients $\omega_i^{(1)}$ are relatively small, whereas for the one with small derivatives, the values of the weighted coefficients $\omega_i^{(1)}$ are large accordingly.

https://doi.org/10.4208/cicp.OA-2017-0039 Published online by Cambridge University Press

The nonlinear weighted coefficients are very effective in capturing shock waves and suppressing numerical oscillations near discontinuities. However, it cannot preserve numerical accuracy, especially for high-order schemes. If we adopt the weighted coefficients in Eq. (3.3), for the second-order scheme, it may not evidently impact the numerical accuracy, but for the high-order schemes, the accuracy will be damaged in smooth regions. The reason is when the flowfield is smooth, the standard deviation coefficients of the reconstruction stencil are all very small and approximately equal. In this circumstance, the nonlinear average in Eq. (3.3) transforms to algebraic average of all the derivatives for each cell, which has little influence on numerical accuracy when the reconstruction stencil is small. However, for the high-order finite volume schemes on unstructured grids, the algebraic average will extremely reduce the accuracy of derivatives of flow variables, since the reconstruction stencil is usually very large.

Therefore, in order to emphasize the importance of the central cell, we further introduce another weighted coefficients related to geometric distance $\omega_i^{(2)}$, which can be expressed as follows

$$\begin{aligned} &\omega_i^{(2)}=\left(\frac{1}{D_i/D_{avg}}\right)^{S(\chi_{central})}, \quad S(\chi_{central})=\min\left(\frac{\varepsilon}{\chi_{central}+\delta},10\right), \\ &D_i=\frac{1}{N}\sum_{m=1}^{N}|\boldsymbol{r}_i-\boldsymbol{r}_m|, \quad D_{avg}=\frac{1}{n}\sum_{i=1}^{n}|\boldsymbol{r}_i-\boldsymbol{r}_{central}|, \end{aligned} \tag{3.4}$$

where D_i denotes the average distance of each cell center $\boldsymbol{r}_i$ in the reconstruction stencil to the face centers $\boldsymbol{r}_m$ of the central cell, and $\boldsymbol{r}=(x,y)$ is the coordinate of each point. D_{avg} is the local distance of the stencil, which is defined by the average distance of the central cell center $\boldsymbol{r}_{central}$ and other cell centers $\boldsymbol{r}_i$ in the stencil. $\chi_{central}$ denotes the standard deviation coefficient of the central cell, and $S(\chi_{central})$ is a function of $\chi_{central}$. δ is a tolerance to avoid being divided by zero, which can be set as 10^{-8}. ε is a free control parameter, the range span of which is proposed to be $[0,0.1]$. N denotes the number of faces for an element, and n is the number of cells in a stencil. Since $S(\chi_{central})$ is the exponent of the distance, considering the maximum digit of the computer, we limit the upper bound of $S(\chi_{central})$ to 10 in order to avoid data overflow. The functions $S(\chi_{central})$ ranging in reference to $\chi_{central}$ with different control parameters are shown in Fig. 2. In smooth regions of the flowfield, the standard deviation coefficients are very small, and the values of $S(\chi_{central})$ are close to 10. Therefore, the proportion of the central cell in the reconstruction stencil is relatively large, which can effectively preserve numerical accuracy in smooth regions. In the discontinuous regions, the values of $S(\chi_{central})$ are very small, and the weighted coefficients $\omega_i^{(2)}$ have small effect, which can suppress the oscillations near discontinuities. We can further see from Fig. 2 that the control parameter ε could also affect the results. When the value of ε is large, the slope of $S(\chi_{central})$ is steep, which will benefit numerical accuracy. However, a small value of is better for suppressing oscillations near discontinuities.

In order to further enhance the robustness of the developed limiter, we do not directly

https://doi.org/10.4208/cicp.OA-2017-0039 Published online by Cambridge University Press

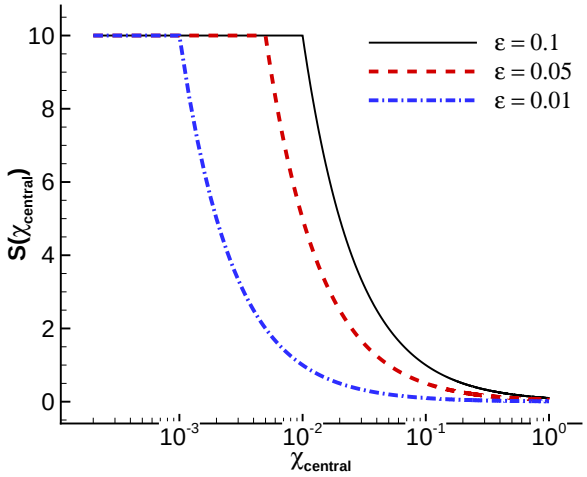


Figure 2: The curves of $S(\chi_{central})$ via $\chi_{central}$ with different control parameters.

apply the weighted coefficients in the derivatives of flow variables, while an extra nonlinear transformation is carried out on all the derivatives referring the conception of the BAP limiter. That is, we first transform the derivatives of flow variables with a kind of biased function, and then reduce the real derivatives by the inverse transformation with the self-similar function. The nonlinear transformation does not degenerate numerical accuracy, on the contrary, it can improve the stability of the flow solver. Therefore, the final expression of the developed DDWENO limiter is as follows

$$\widetilde{g_{central}} = L(g_1, g_2, \cdots, g_n) = B^{-1}\left(\sum_{i=1}^{n} \omega_i^{(1)} \omega_i^{(2)} B(g_i)\right), \tag{3.5}$$

where $\omega_i^{(1)}$ and $\omega_i^{(2)}$ are defined by the Eq. (3.3) and Eq. (3.4), and the nonlinear transformation function and its self-similar function adopted are in the following

$$B(x) = \frac{x}{\sqrt{1+x^2}}, \quad B^{-1}(x) = \frac{x}{\sqrt{1-x^2}}. \tag{3.6}$$

Now, we briefly analyze the mechanism of the developed DDWENO limiter below. Fig. 3 shows the stencils of the DDWENO limiter for the second-, third-order and fourth-order schemes. The cells surrounded by black solid lines denote the stencil used in limiting step for the central cell i, which is the same fixed stencil in initial k-exact reconstruction step. For the second-order scheme, we directly choose the face neighbor cells as the reconstruction stencil, and for the high-order schemes, we extend the face neighbor cells in the same way as the second-order scheme. Although the fixed stencil is used in limiting step, when computing the standard deviation coefficients in k-exact reconstruction step, we implement it based on the stencil centered by each cell as shown in Fig. 3 surrounded by the dashed lines. The value of the standard deviation coefficient

https://doi.org/10.4208/cicp.OA-2017-0039 Published online by Cambridge University Press

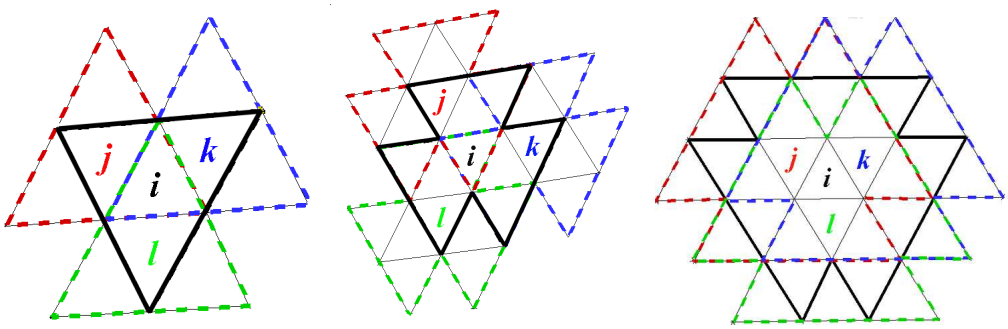


Figure 3: The stencils of the DDWENO limiter for the second-, third-order and fourth-order schemes.

represents the smoothness for the stencil that is centered by each cell. Therefore, weighting all the derivatives by the standard deviation coefficient of each cell is equivalent to weighting all the stencils centered by each cell i,j,k and l (To avoid view confusion, we do not show all the stencils for the third-order and the fourth-order scheme in Fig. 3). The developed DDWENO limiter can be considered as the combination of the slope limiter and the WENO scheme, which is ingeniously designed to avoid the complexity of choosing large number of candidate stencils, while it can achieve similar effect as the WENO scheme on the fixed reconstruction stencil. So the DDWENO limiter has high computational efficiency and is simple to be implemented on unstructured grids. Meanwhile, by introducing the weighted coefficients of the distance, the numerical accuracy can be also preserved in smooth regions.

4 Numerical tests

4.1 Inviscid isentropic vortex flow

Inviscid isentropic flow [14,31] is a typical flow to test the resolution of numerical methods. For the Euler equations in two-dimension: the mean flow is $\rho_\infty=1$, $u_\infty=v_\infty=1$, $p_\infty=1$. In initial conditions, an isentropic vortex with no perturbation in entropy is added to the mean flowfield. The perturbations of velocity and temperature are given by

$$(\delta u,\delta v)=\frac{\tau}{2\pi}e^{\frac{(1-\gamma^2)}{2}}(-\overline{y},\overline{x}), \tag{4.1}$$

$$\delta T=\frac{(\gamma-1)\tau^2}{8\gamma\pi^2}e^{1-\gamma^2},\quad \delta S=0, \tag{4.2}$$

where τ is the vortex strength, $\gamma=1.4$, $T=p/\rho$ and $r=\sqrt{\overline{x}^2+\overline{y}^2}$, where $(\overline{x},\overline{y})=(x-x_0,y-y_0)$. From $\rho=\rho_\infty+\delta\rho$, $u=u_\infty+\delta u$,$v=v_\infty+\delta v$,$T=T_\infty+\delta T$, and the isentropic relation, other

https://doi.org/10.4208/cicp.OA-2017-0039 Published online by Cambridge University Press

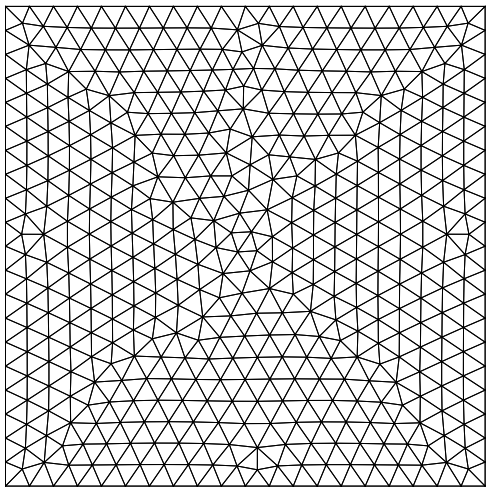


Figure 4: The computational grid size of 1/2 for inviscid isentropic vortex flow.

flow variables can be obtained by

$$\rho = T^{1/(\gamma-1)} = (T_\infty + \delta T)^{1/(\gamma-1)} = \left[1 - \frac{(\gamma-1)\tau^2}{8\gamma\pi^2} e^{1-\gamma^2}\right]^{1/(\gamma-1)}, \tag{4.3}$$

$$p = \rho^\gamma. \tag{4.4}$$

The computational domain is set as $(x,y) \in [0,10] \times [0,10]$, in which a series of five quasi-uniform triangular meshes are generated, ranging in size of 1/1, 1/2, 1/4, 1/8 and 1/16. The computational grid size of 1/2 is shown in Fig. 4. Both boundaries of the domain are set with periodic boundary conditions. In order to avoid additional errors, the initial mean flow variables in computational domain are assigned by five-order accuracy Gauss integral formula. We set the control parameter $\varepsilon = 0.1$ and compute the solution up to $t = 2.0$. The errors of density in terms of L_1, L_2 and L_∞ norms computed by the BAP and the DDWENO limiter are shown in Fig. 5, and the orders of accuracy are compared in Table 1. The errors of L_1, L_2 and L_∞ norms are defined as:

$$\begin{aligned} \|\varepsilon\|_{L_1} &= \frac{1}{n}\sum_{i=1}^{n} |u_{cal} - u_{exact}|, \\ \|\varepsilon\|_{L_2} &= \frac{1}{n}\sum_{i=1}^{n} \sqrt{(u_{cal} - u_{exact})^2}, \\ \|\varepsilon\|_{L_\infty} &= \max_{1\le i\le n} |u_{cal} - u_{exact}|, \end{aligned} \tag{4.5}$$

where u_{cal} denotes numerical values, and u_{exact} denotes analytical values.

The results indicate, for the third- and fourth-order schemes, the numerical accuracy is seriously impacted by using the BAP limiter, and the higher the order is, the larger the

https://doi.org/10.4208/cicp.OA-2017-0039 Published online by Cambridge University Press

Table 1: Density errors and accuracy orders for inviscid isentropic vortex flow.

	Mesh	L_1error	Order	L_2error	Order	$L_\infty error$	Order
no limiter-2nd	1/1	8.149E-03		1.472E-02		8.117E-02	
	1/2	1.827E-03	2.17	3.444E-03	2.11	3.321E-02	1.30
	1/4	4.608E-04	2.06	8.505E-04	2.09	7.041E-03	2.32
	1/8	9.266E-05	2.23	1.686E-04	2.25	1.833E-03	1.87
	1/16	2.231E-05	2.06	4.047E-05	2.06	4.562E-04	2.01
BAP-2nd	1/1	8.802E-03		2.094E-02		1.416E-01	
	1/2	2.147E-03	2.05	4.854E-03	2.12	4.045E-02	1.82
	1/4	5.505E-04	2.04	1.357E-03	1.91	1.410E-02	1.58
	1/8	1.197E-04	2.12	2.827E-04	2.18	2.676E-03	2.31
	1/16	2.761E-05	2.12	6.507E-05	2.12	7.841E-04	1.77
DDWENO-2nd	1/1	7.676E-03		1.434E-02		9.085E-02	
	1/2	1.801E-03	2.10	3.424E-03	2.08	3.299E-02	1.47
	1/4	4.603E-04	2.04	8.507E-04	2.08	7.065E-03	2.31
	1/8	9.266E-05	2.23	1.686E-04	2.25	1.833E-03	1.87
	1/16	2.231E-05	2.06	4.047E-05	2.06	4.562E-04	2.01
no limiter-3rd	1/1	8.844E-03		2.107E-02		1.416E-01	
	1/2	1.805E-03	2.30	4.541E-03	2.23	3.343E-02	2.09
	1/4	3.416E-04	2.49	8.742E-04	2.47	6.341E-03	2.49
	1/8	4.247E-05	2.90	1.058E-04	2.90	8.709E-04	2.76
	1/16	5.565E-06	2.93	1.397E-05	2.92	1.168E-04	2.90
BAP-3rd	1/1	1.293E-02		3.118E-02		2.152E-01	
	1/2	3.308E-03	1.98	8.519E-03	1.88	6.944E-02	1.64
	1/4	8.152E-04	2.10	2.157E-03	2.06	2.596E-02	1.47
	1/8	1.320E-04	2.53	3.871E-04	2.39	6.554E-03	1.91
	1/16	2.128E-05	2.64	6.754E-05	2.52	1.159E-03	2.50
DDWENO-3rd	1/1	9.823E-03		2.390E-02		1.598E-01	
	1/2	2.367E-03	2.06	6.131E-03	1.97	4.925E-02	1.71
	1/4	4.181E-04	2.59	1.107E-03	2.56	8.739E-03	2.59
	1/8	4.307E-05	3.16	1.075E-04	3.24	9.089E-04	3.15
	1/16	5.567E-06	2.95	1.397E-05	2.95	1.158E-04	2.97
no limiter-4th	1/1	4.574E-03		9.443E-03		6.192E-02	
	1/2	5.982E-04	2.95	1.432E-03	2.73	1.347E-02	2.21
	1/4	4.209E-05	3.97	9.023E-05	4.14	6.328E-04	4.58
	1/8	2.052E-06	4.20	4.173E-06	4.27	2.933E-05	4.27
	1/16	1.325E-07	3.96	3.013E-07	3.80	1.951E-06	3.91
BAP-4th	1/1	1.411E-02		3.365E-02		2.332E-01	
	1/2	3.604E-03	1.98	9.158E-03	1.89	7.290E-02	1.69
	1/4	1.057E-03	1.83	2.868E-03	1.74	3.963E-02	0.91
	1/8	1.999E-04	2.32	6.383E-04	2.09	1.089E-02	1.80
	1/16	3.405E-05	2.56	1.203E-05	2.41	1.979E-03	2.46
DDWENO-4th	1/1	6.484E-03		1.494E-02		1.059E-01	
	1/2	2.244E-03	1.54	6.132E-03	1.29	6.119E-02	0.80
	1/4	1.676E-04	3.88	5.325E-04	3.66	9.489E-03	2.79
	1/8	2.421E-06	5.89	5.549E-06	6.34	6.211E-05	6.99
	1/16	1.358E-07	4.16	3.159E-07	4.14	6.026E-06	3.37

https://doi.org/10.4208/cicp.OA-2017-0039 Published online by Cambridge University Press

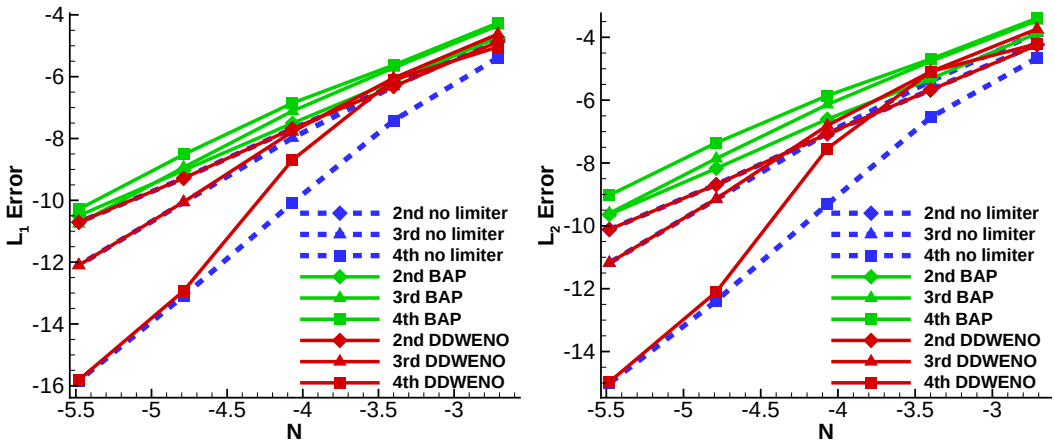


Figure 5: Accuracy comparison of the BAP limiter, the DDWENO limiter and no limiter for inviscid isentropic vortex flow.

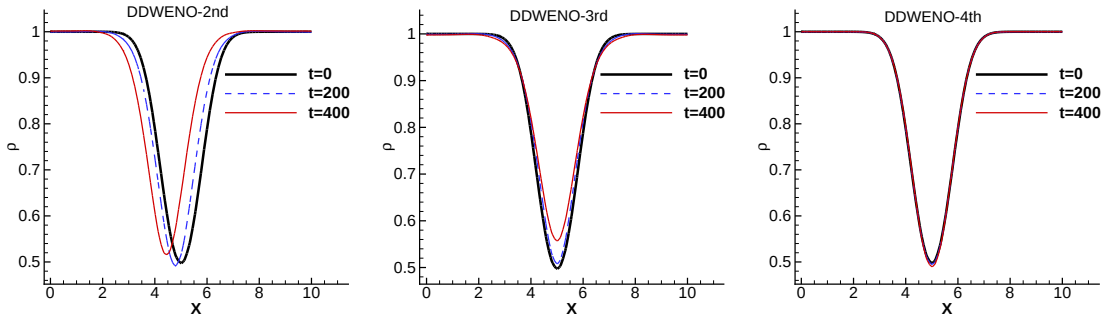


Figure 6: Density distributions along x-axis at $t=0$, $t=200$ and $t=400$ using different orders of schemes by the DDWENO limiter for inviscid isentropic vortex flow.

computational errors will be obtained. The reason is that when the reconstruction stencil is extended for high-order scheme, the algebraic mean of the derivatives will damage the numerical accuracy in smooth regions. However, the developed DDWENO limiter, for all the second-, third- and fourth-order schemes, can achieve the analytical orders of accuracy, and the absolute errors are slightly larger than the situation without limiter.

In order to further study the influence of the DDWENO limiter on numerical dissipation and dispersion, we focus on the grid size of $1/8$, and compute the solution up to $t=200$ and $t=400$ respectively. The distributions of density along x-axis for the second-, third- and fourth-order schemes by the DDWENO limiter are shown in Fig. 6. It can be clearly seen, for the second-order scheme, both the numerical dissipation and the dispersion are relatively large. The density of the vortex center increases apparently and its position shifts away from the initial center. For the third-order scheme, the dissipation can be noticeably seen from the results, and the density of the vortex center also increases, but its position is accurate. However, for the fourth-order scheme, both the dissipation

https://doi.org/10.4208/cicp.OA-2017-0039 Published online by Cambridge University Press

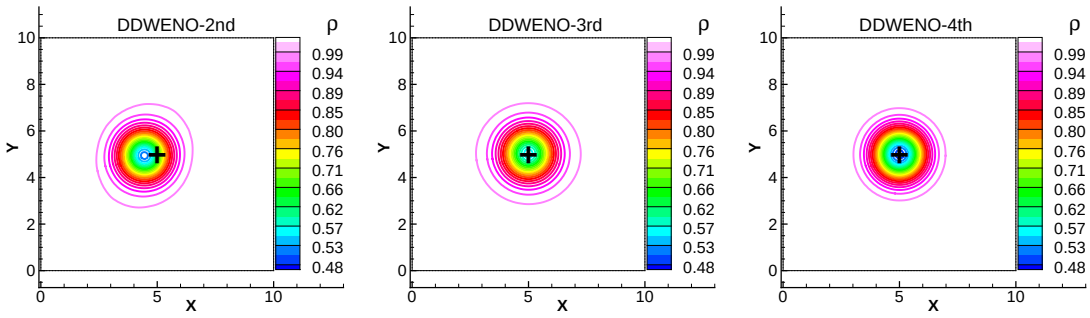


Figure 7: The location and the shape of the vortex at $t=400$ using different orders of schemes by the DDWENO limiter for inviscid isentropic vortex flow.

and the dispersion are very small, and the density along x-axis is almost the same as the initial one, even at $t=400$. Fig. 7 displays the shape and the position of the isentropic vortex at $t=400$ for the second-, third- and fourth-order schemes by the DDWENO limiter, where the symbol "+" shows the initial position of the vortex. It obviously indicates that high-order scheme can achieve more precise results.

4.2 Shock tube problems

This test is used to examine the capability of the developed DDWENO limiter for capturing contact discontinuity on unstructured grids. The Sod's shock tube and the Lax shock tube problems are implemented in this section. The initial conditions are Sod problem:

$$(\rho,u,p)=\begin{cases}(1.0,0,1.0), & x\leq 0.5,\\ (0.125,0,0.1), & x>0.5;\end{cases} \tag{4.6}$$

Lax problem:

$$(\rho,u,p)=\begin{cases}(0.445,0.698,3.528), & x\leq 0.5,\\ (0.5,0,0.571), & x>0.5.\end{cases} \tag{4.7}$$

The computational domain is set as $(x,y)\in[0,1]\times[0,0.2]$, and we use the unstructured grids with the scale of $h=1/200$, which is shown in Fig. 8. We compute the solution up to $t=0.2$ for the Sod problem, and $t=0.1$ for the Lax problem. The control parameter is set as $\varepsilon=0.1$ and $\varepsilon=0.01$ respectively, and the results of density distributions along the x-axis for the third- and fourth-order schemes are displayed in Fig. 9 and Fig. 10. In all, the developed DDWENO limiter can steeply capture contact discontinuities. Slight numerical oscillations can be observed, but they are nearly eliminated by reconstructing characteristic variables.

https://doi.org/10.4208/cicp.OA-2017-0039 Published online by Cambridge University Press

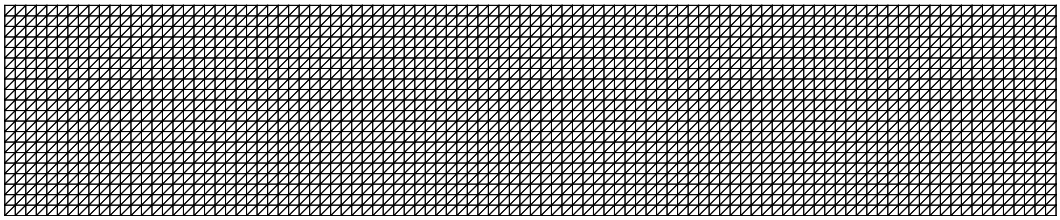


Figure 8: The computational grids for the shock tube problems.

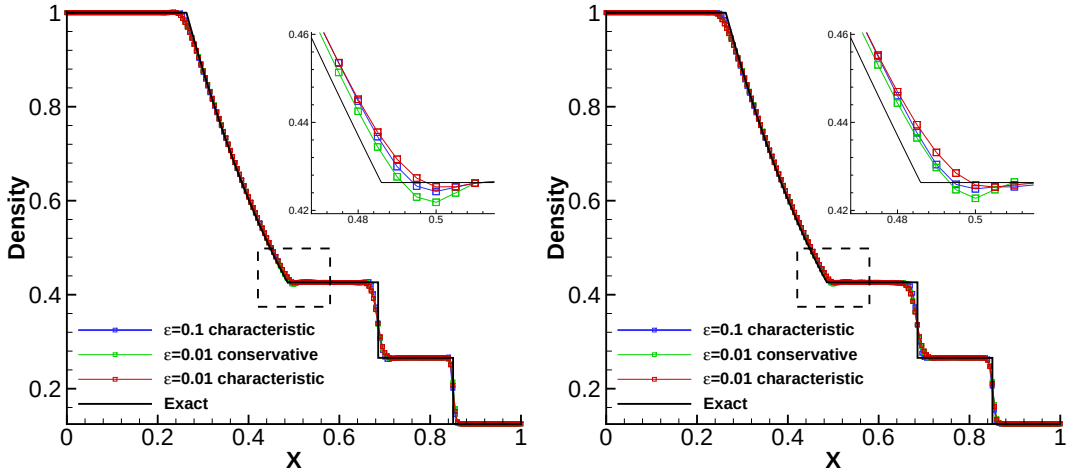


Figure 9: Density distributions along the x-axis for the Sod problem. Left: 3rd order; Right: 4th order.

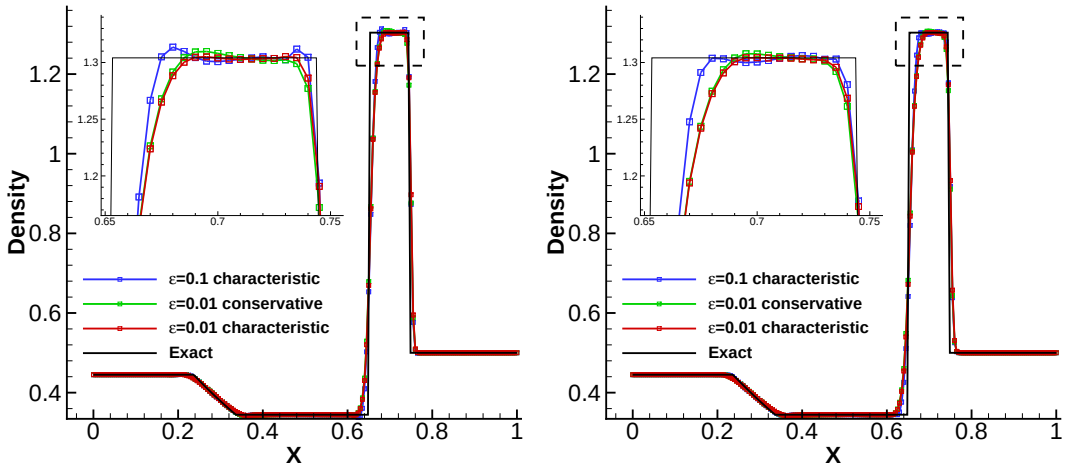


Figure 10: Density distributions along the x-axis for the Lax problem. Left: 3rd order; Right: 4th order.

https://doi.org/10.4208/cicp.OA-2017-0039 Published online by Cambridge University Press

4.3 Transonic inviscid flow past a NACA0012 airfoil

The transonic inviscid flow past a NACA0012 airfoil is used to evaluate the performance of the developed DDWENO limiter. The computational mesh is shown in Fig. 11, which consists of 7038 triangular elements and 200 boundary points on the airfoil surface. The free stream Mach number is $Ma = 0.8$ and the angle of attack is $\alpha = 0.125^\circ$. We set the limiter control parameter as $\varepsilon = 0.1$. Fig. 12 compares thirty pressure isolines computed respectively by the third- and the fourth-order schemes with the DDWENO limiter. Fig. 13 compares the pressure coefficients and the convergence histories computed by the second-, third- and fourth-order schemes. The results indicate that, the numerical oscillations near discontinuities can be effectively controlled, and the shock waves can be steeply captured with high resolution. We can also see that the DDWENO limiter has a

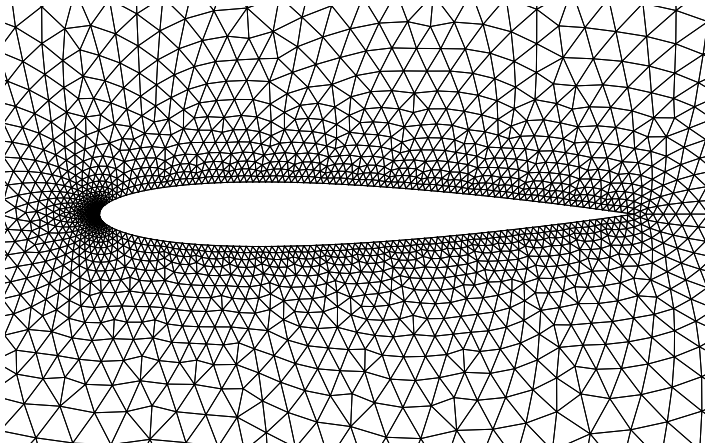


Figure 11: Grids near the NACA0012 airfoil surface.

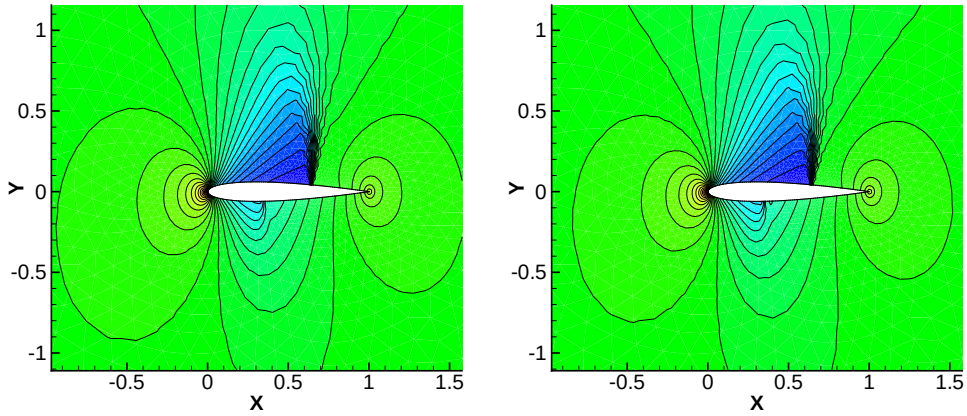


Figure 12: Pressure isolines near the NACA0012 airfoil computed by DDWENO limiter (Left: third-order scheme; Right: fourth-order scheme).

https://doi.org/10.4208/cicp.OA-2017-0039 Published online by Cambridge University Press

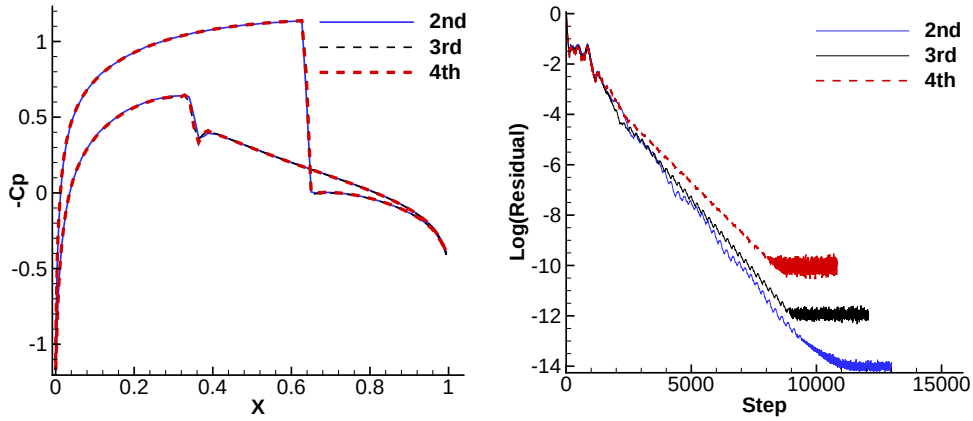


Figure 13: Comparison of pressure coefficients of the NACA0012 airfoil and the convergence histories by the DDWENO limiter for different orders of accuracy.

good performance in convergence to steady state, of which it converges to machine zero for the second-order scheme, and declines more than ten orders of the magnitude for the third- and fourth-order schemes.

Fig. 14 compares the entropy production distributions obtained by different orders of accuracy with the DDWENO limiter. The entropy productions are all very small, and the numerical oscillations can be effectively controlled near the strong shock wave on the upper surface of the airfoil, while slight fluctuation emerges near the wake shock on the lower surface because of the low numerical dissipation. The comparison of the computed lift and drag coefficients with reference data are displayed in Table 2. The results by using the DDWENO limiter present good agreement with the data given in the references.

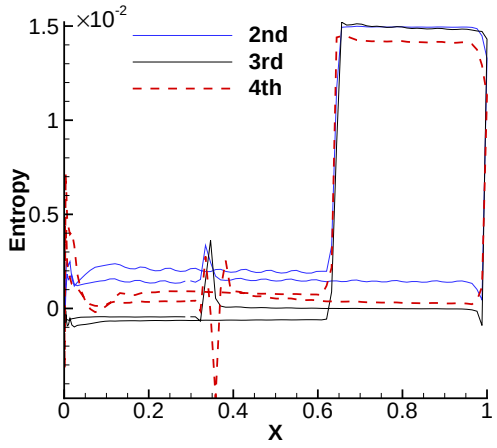


Figure 14: Comparison of the computed entropy production distributions on the surface of the NACA0012 airfoil obtained by the second-, third- and fourth-order schemes with the DDWENO limiter.

https://doi.org/10.4208/cicp.OA-2017-0039 Published online by Cambridge University Press

Table 2: Comparison of the computed lift and drag coefficients with reference data for transonic flow past a NACA0012 airfoil at $Ma=0.8$, $\alpha=1.25^\circ$.

	C_l	C_d
DDWENO-2nd	0.34532	0.02320
DDWENO-3rd	0.35022	0.02300
DDWENO-4th	0.35020	0.02307
MLP-u2 limiter (Park [31])	0.3452	0.0217
AGARD 211 [44]	0.3463	0.0223
Vassberg&Jameson [45] (very fine mesh, 16.8 million)	0.3562	0.0227

4.4 Transonic flow past a RAE2822 airfoil

The test of transonic flow past a RAE2822 airfoil is used to compare the effect of different limiters. The computational mesh is shown in Fig. 15, which consists of 5316 triangular elements and 200 boundary points on the airfoil surface. The free stream Mach number is $Ma=0.75$ and the angle of attack is $\alpha=3^\circ$. We set the limiter control parameter as $\varepsilon=0.1$. Fig. 16 shows the pressure isolines and the standard deviation coefficients of the flowfield computed by the third-order scheme with the DDWENO limiter. The smoothness indicator can accurately detect the shock wave on the upper surface of the airfoil, and the value of which is close to zero in smooth regions. Fig. 17 compares the pressure coefficient distributions on the surface of RAE2822 airfoil by the Barth&Jespersen limiter, the Venkataksrishnan limiter, the BAP limiter and the developed DDWENO limiter with the reference data. The DDWENO limiter has a good effect on suppressing non-physical oscillations near the shock wave. Fig. 18 and Fig. 19 display the convergence histories of the flowfield and the distributions of the entropy production on the RAE2822 airfoil surface computed by different limiters respectively. As is shown in the results, the convergence history is stalled by the Barth&Jespersen limiter after a drop of about three orders

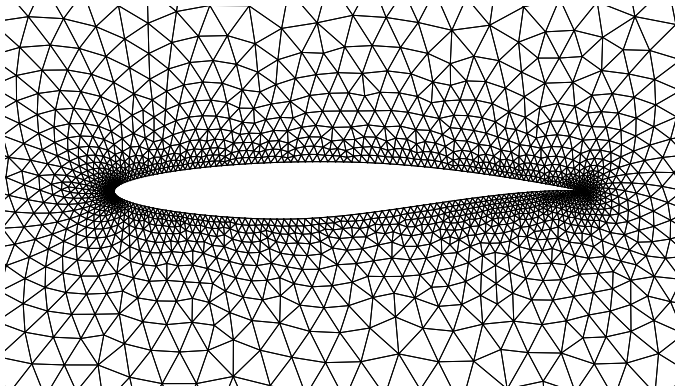


Figure 15: The computational grids of RAE2822 airfoil.

https://doi.org/10.4208/cicp.OA-2017-0039 Published online by Cambridge University Press

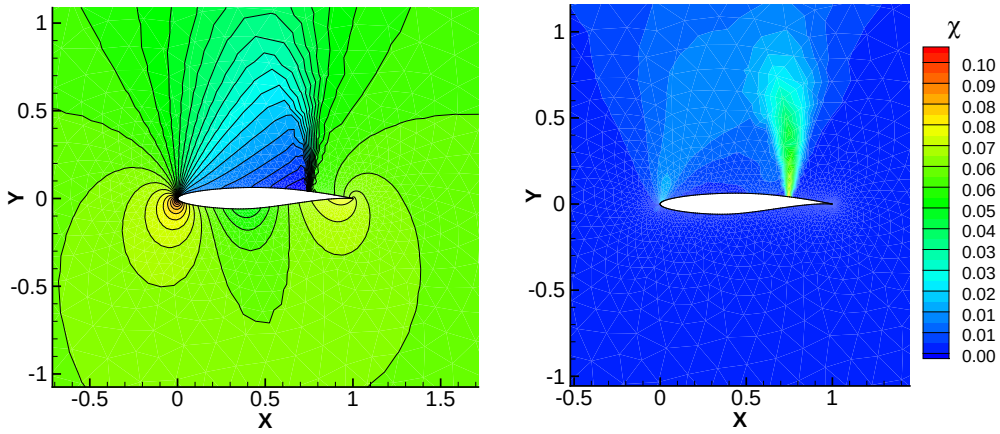


Figure 16: Pressure isolines (left) and the standard deviation coefficients (right) of the flowfield computed with the DDWENO limiter for the case of the RAE2822 airfoil.

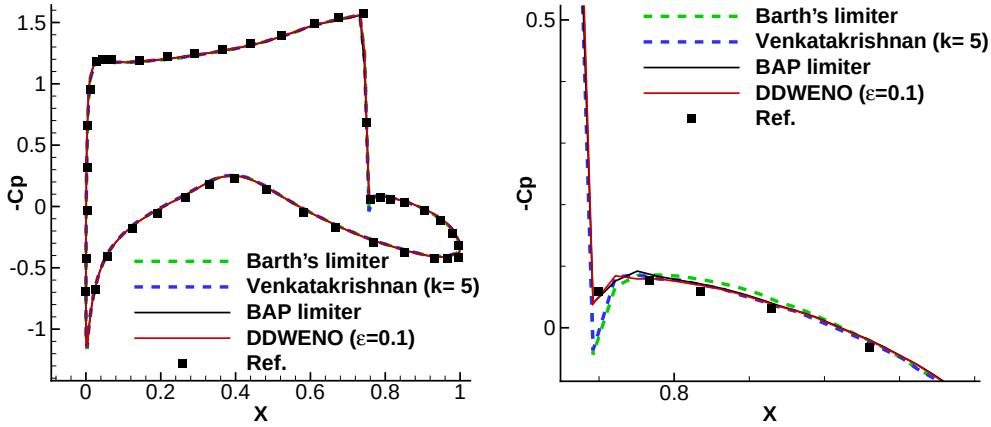


Figure 17: Pressure coefficient distributions on the RAE2822 airfoil surface and the partial zoomed view near the shock wave computed by different limiters.

of magnitude. For the Venkataksrishnan limiter, although the residual errors can drop down to machine zero, the numerical oscillations cannot be completely controlled near the shock wave. Besides, the limiter is very sensitive to the free parameter. If the free parameter decreases, the convergence history of the Venkataksrishnan limiter will also stall just as the Barth&Jespersen limiter shows. In comparison with the existed limiters, the developed DDWENO limiter has smaller entropy production and lower numerical dissipation, which can also effectively suppress the oscillations near the shock wave on the upper surface of the RAE2822 airfoil. Table 3 displays the lift and drag coefficients calculated by different limiters, and the results by the DDWENO limiter also agree quite well with the reference data.

https://doi.org/10.4208/cicp.OA-2017-0039 Published online by Cambridge University Press

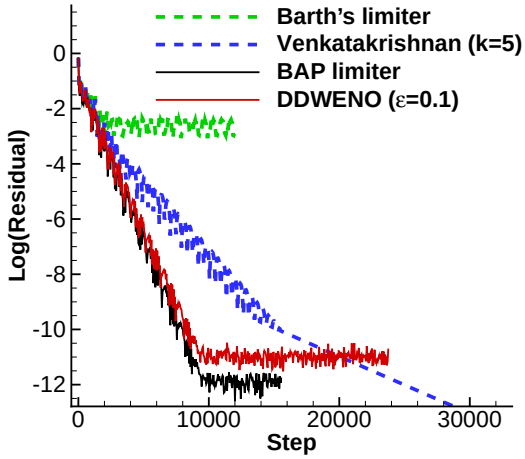


Figure 18: The convergence histories by using different limiters for the case of transonic flow past a RAE2822 airfoil.

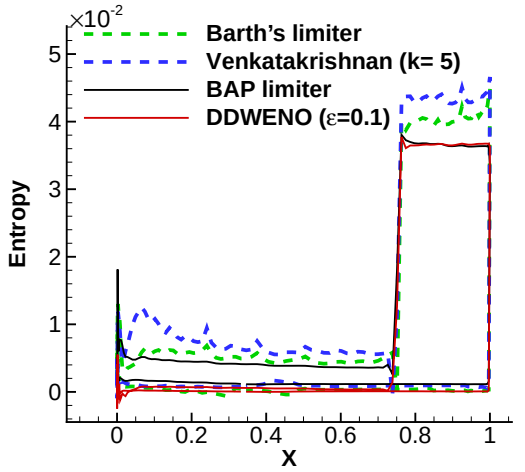


Figure 19: The distributions of the entropy production on the RAE2822 airfoil surface of different limiters.

Table 3: Comparison of the computed lift and drag coefficients with reference data for the transonic flow past a RAE2822 airfoil.

	C_l	C_d
Barth's limiter	1.09161	0.04526
Venkatakrishnan($k=5$)	1.08912	0.04518
BAP limiter	1.09432	0.04481
DDWENO ($\varepsilon=0.1$)	1.09764	0.04446
Jameson [8]	1.1227	0.0460

https://doi.org/10.4208/cicp.OA-2017-0039 Published online by Cambridge University Press

4.5 A Mach 3 wind tunnel with a step

This is a typical case for testing high-resolution schemes [46]. The computational domain is $x \in [0,3], y \in [0,1]$. The step is 0.2 length units high and is located at 0.6 length unites from the left end of the tunnel. Uniform Mach 3 flow impacts the step, and the initial conditions are $(\rho,u,v,p)=(1.4,3.0,0,1.0)$. The mesh scale of $\Delta h=1/120$ is used, and the grids near the step corner are refined, which is shown in Fig. 20. First, we set the control parameter as $\varepsilon=0.1$ and compute the solution up to $t=4$. The density contours and the standard deviation coefficients of the flowfield calculated by the second-, third- and fourth-order schemes with the DDWENO limiter are presented in Fig. 21. It demonstrates that the standard deviation coefficients can give an accurate description of complex shock waves. In comparison with the second- and third-order schemes, the fourth-order scheme can capture shock waves more clearly with higher resolution.

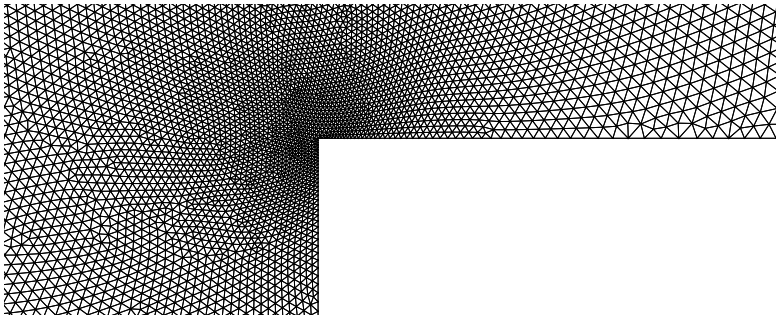


Figure 20: The computational grids near the step corner for the case of a Mach 3 wind tunnel with a step.

For the fourth-order scheme, we re-compute the case by setting the control parameter as $\varepsilon=0$, 0.01 and 0.05 respectively. The density contours and the distributions of the vorticity computed by the fourth-order scheme with the DDWENO limiter are shown in Fig. 22. It can be seen that the developed DDWENO limiter is not very sensitive to the control parameter. When ε is large, more precision and higher resolution can be achieved; while ε is small, the numerical process is more robust and has a better convergence feature.

4.6 Double Mach reflection

This is one of the most popular test cases for high-resolution schemes [45]. The computational domain is $[0,4]\times[0,1]$. The wall is located at the bottom of the computational domain beginning at $x=1/6$. Initially a right-moving Mach 10 shock is positioned at $x=1/6$, $y=0$ and make a 60° angle with the x-axis. For the bottom boundary, the exact post-shock condition is imposed for the part from $x=0$ to $x=1/6$, and a reflective boundary condition is used for the rest. At the top boundary, the flow values are set to describe the exact motion of the initial Mach 10 shock. We compute the solution up to $t=2$.

https://doi.org/10.4208/cicp.OA-2017-0039 Published online by Cambridge University Press

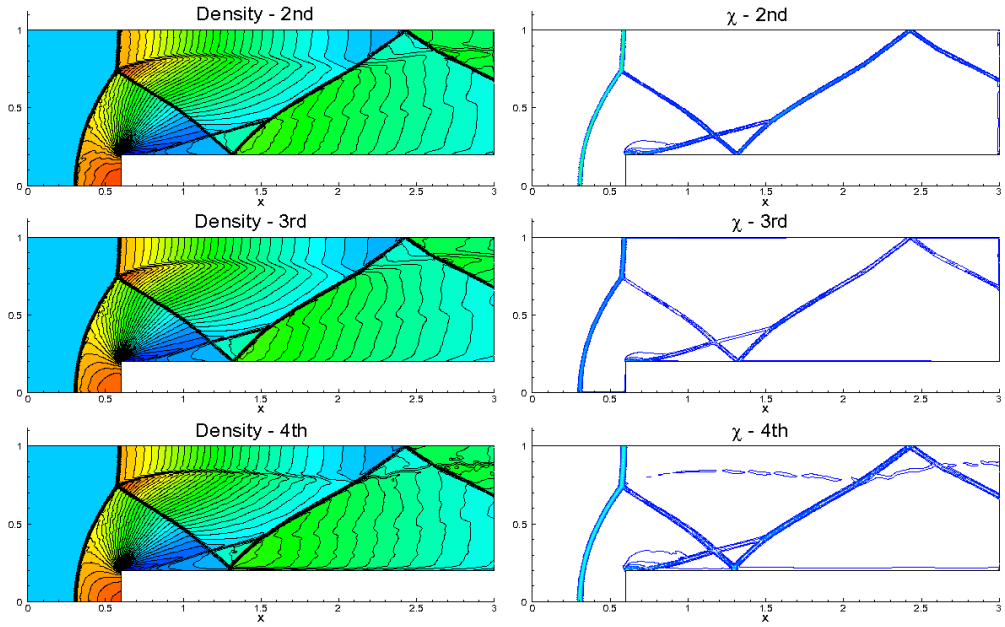


Figure 21: Density contours and the distributions of standard deviation coefficients of the flowfield computed by the second-, third- and fourth-order schemes with DDWENO limiter.

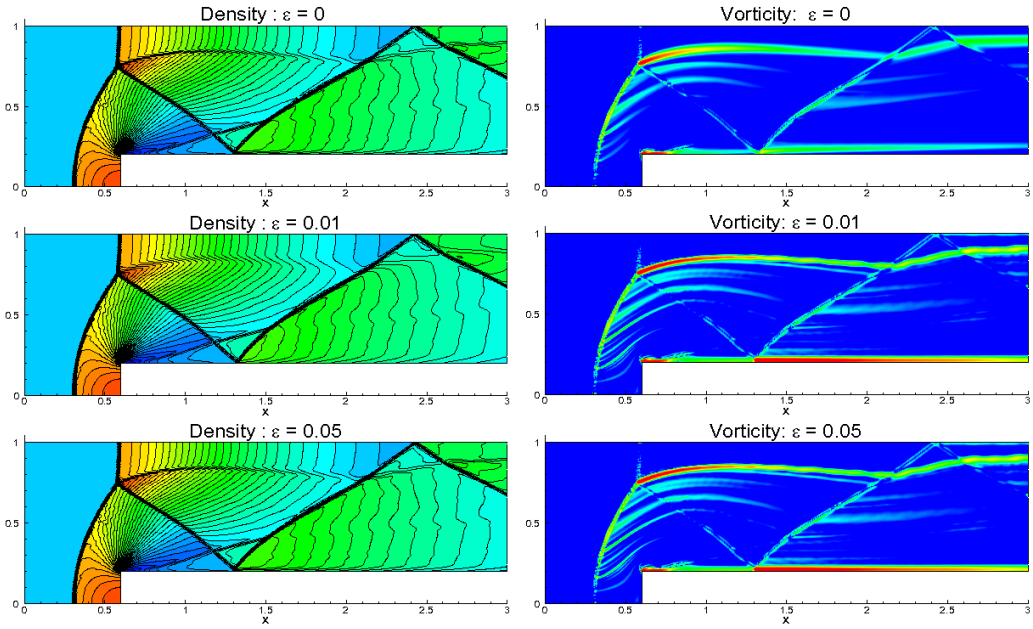


Figure 22: Density contours and the distributions of the vorticity computed by the fourth-order scheme with different control parameters of the DDWENO limiter for the case of a Mach 3 wind tunnel with a step.

https://doi.org/10.4208/cicp.OA-2017-0039 Published online by Cambridge University Press

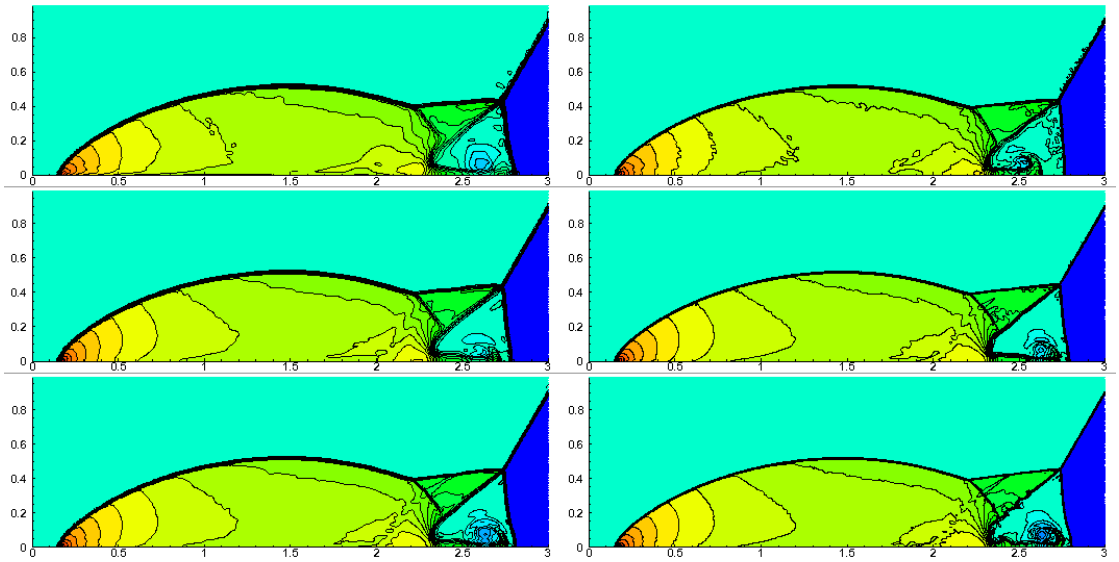


Figure 23: Comparison of density contours for double Mach reflection. Thirty equally spaced contour lines from $\rho=2.0$ to 22.0. (Left: $h=1/120$; right: $h=1/240$; up: 2nd order; middle: 3rd order; down: 4th order).

Fig. 23 and Fig. 24 show the density contours calculated on the mesh with grid size $h=1/120$ and $h=1/240$, respectively. The second-, third- and fourth-order DDWENO limiters with the control parameter $\varepsilon=0.1$ are applied for the problem. From the results, we can see that the developed DDWENO limiter is robust for capturing strong shock waves. Moreover, the fourth-order scheme shows the complicated shock structure near the Mach stem much more clearly than the lower schemes.

5 Conclusions

A robust and accurate DDWENO limiter has been developed for the second- and high-order finite volume methods on unstructured grids. The novel limiter is based on the k-exact reconstruction method and combines the conceptions of the slope limiter and the WENO type scheme, which can successfully avoid the complexity in choosing large number of candidate stencils, and achieve similar effectiveness as the WENO scheme on the fixed reconstruction stencil. The numerical results for a number of test cases demonstrate that the DDWENO limiter can maintain high-order accuracy and capture discontinuities sharply, and has a good convergence property. Furthermore, the developed limiter is not very sensitive to the free control parameter, which has a good effect on controlling non-physical oscillations by modulating the parameter. Besides, the DDWENO limiter also has high computational efficiency, and is simple to be implemented on unstructured grids for high-order and high-dimensional cases, which exhibits great potential in extensive applications.

https://doi.org/10.4208/cicp.OA-2017-0039 Published online by Cambridge University Press

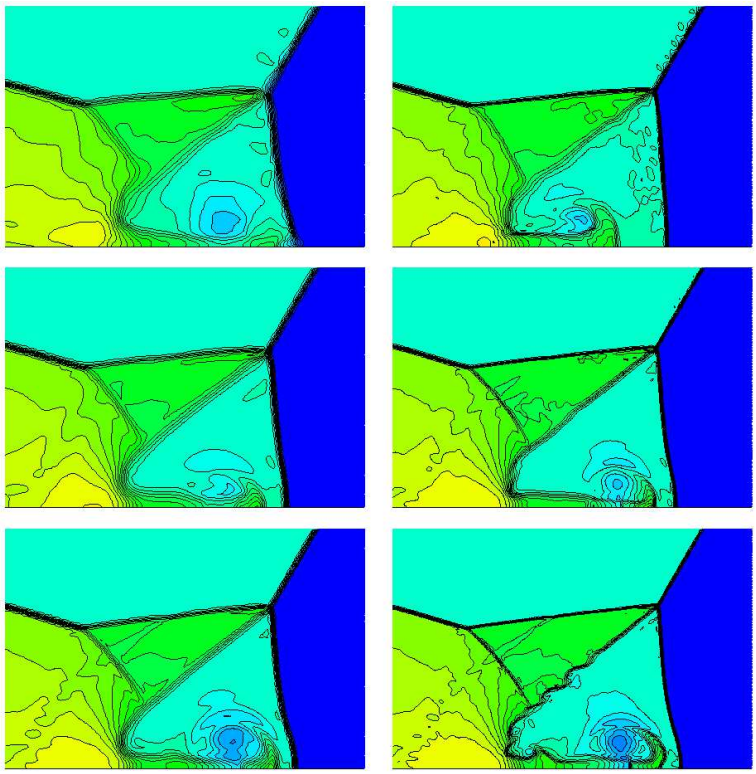


Figure 24: Close-up view around the double Mach stem. (Left: $h=1/120$; right: $h=1/240$; up: 2nd order; middle: 3rd order; down: 4th order).

Acknowledgments

This work was supported by the National Science Fund for Excellent Young Scholars (No. 11622220) and the ATCFD project (No. 2015-F-016) and the "111" project of China (No. B17037).

References

[1] Gao C Q, Zhang W W, Li X T, et al. Mechanism of frequency lock-in in transonic buffeting flow. Journal of Fluid Mechanics, 2017, 818: 528-561.
[2] Kou J Q, Zhang W W. An improved criterion to select dominant modes from dynamic mode decomposition. European Journal of Mechanics B/Fluids, 2017, 62: 109-129.
[3] Kou J Q, Zhang W W, Liu Y L, et al. The lowest Reynolds number of vortex-induced vibrations. Physics of Fluids, 2017, 29: 041701.
[4] Li J, Zhong C W, Wang Y, et al. Implementation of dual time-stepping strategy of the gas-kinetic scheme for unsteady flow simulations. Physical Review E, 2017, 5(95): 053307.
[5] Wang Z J. High-order methods for the Euler and Navier-Stokes equations on unstructured grids. Progress in Aerospace Sciences, 2007, 43: 1-41.

https://doi.org/10.4208/cicp.OA-2017-0039 Published online by Cambridge University Press

[6] Ollivier-Gooch C, Nejat A, Michalak K. Obtaining and verifying high-order unstructured finite volume solutions on the Euler equations. AIAA Journal, 2009, 47(9): 2105-2120.
[7] Liu Y L, Zhang W W, Jiang Y W, et al. A high-order finite volume method on unstructured grids using RBF reconstruction. Computers and Mathematics with Applications, 2016, 72: 1096-1117.
[8] Jameson A. Analysis and design of numerical schemes for gas dynamics, 1: artificial diffusion, upwind biasing, limiters and their effect on accuracy and multigrid convergence. International Journal of Computational Fluid Dynamics, 1995, 4(3-4): 171-218.
[9] Jameson A, Schmidt W, Turkel E. Numerical solutions of the Euler equations by finite volume methods using Runge-Kutta time-stepping schemes. AIAA paper, 1981, 1259: 1981.
[10] Swanson R C, Radespiel R, Turkel E. On some numerical dissipation schemes. Journal of Computational Physics, 1998, 147(2): 518-544.
[11] Harten A. High resolution schemes for hyperbolic conservation laws. Journal of Computational Physics, 1983, 49(3): 357-393
[12] Harten A, Engquist B, Osher S, et al. Uniformly high-order essentially non-oscillatory schemes, III. Journal of Computational Physics, 1997, 131: 3-47.
[13] Friedrich O. Weighted essentially non-oscillatory schemes for the interpolation of mean values on unstructured grids. Journal of Computational Physics, 1998, 144: 194-212.
[14] Hu C, Shu C W. Weighted essentially non-oscillatory schemes on triangular meshes. Journal of Computational Physics, 1999, 150:97-127
[15] Liu Y, Zhang Y T. A robust reconstruction for unstructured WENO schemes. Journal of Scientific Computing, 2013, 54: 603-621.
[16] Jiang G S, Shu C W. Efficient implementation of Weighted ENO schemes. Journal of Computational Physics, 1996, 126: 202-228.
[17] Shen Y Q, Zha G C, Wang B Y. Improvement of stability and accuracy of implicit WENO scheme, AIAA Journal, 2009, 47: 331-344
[18] Qiu J X, Shu C W. Hermite WENO schemes and their application as limiters for Runge-Kutta discontinuous Galerkin method Π : Two dimensional case. Computers & Fluids, 2005, 34: 642-663.
[19] Luo H, Baum J D, L?hner R. A Hermite WENO-based limiter for discontinuous Galerkin method on unstructured grids. Journal of Computational Physics, 2007, 225: 686-713.
[20] Ivan L, Groth C P T. High-order central ENO finite-volume scheme with adaptive mesh refinement. AIAA 2007-4323, 2007.
[21] Susanto A, Ivan L, Sterck H D, et al. High-order central ENO finite-volume scheme for ideal MHD. Journal of Computational Physics, 2013, 250: 141-164.
[22] Charest M R J, Groth C P T, Gauthier P Q. A high-order central ENO finite-volume scheme for three-dimensional low-speed viscous flows on unstructured mesh. Communications in Computational Physics, 2015, 3(17): 615-656.
[23] Ivan L, Sterck H D, Susanto A, et al. High-order central ENO finite-volume scheme for hyperbolic conservation laws on three-dimensional cubed-sphere grids. Journal of Computational Physics, 2015, 282: 157-182.
[24] Charest M R J, Canfield T R, Morgan N R, et al. A high-order vertex-based central ENO finite-volume scheme for three-dimensional compressible flows. Computers & Fluids, 2015, 114: 172-192.
[25] Barth T J, Jespersen D C. The design and application of upwind schemes on unstructured meshes. AIAA 89-0366, 1989.
[26] Venkatakrishnan, V.: Convergence to Steady-State Solutions of the Euler Equations on Un-

https://doi.org/10.4208/cicp.OA-2017-0039 Published online by Cambridge University Press

structured Grids with Limiters. Journal of Computational Physics, 1995, 118: 120-130.
[27] Michalak C, Ollivier-Gooch C. Accuracy preserving limiter for the high-order accurate solution of the Euler equations. Journal of Computational Physics, 2009, 228: 8693-8711.
[28] Hou J M, Simons F, Mahgoub M, et al. A robust well-balanced model on unstructured grids for shallow water flows with wetting and drying over complex topography. Computer Methods in Applied Mechanics and Engineering, 2013, 257: 126-149.
[29] Kim K H, Kim C. Accurate, efficient and monotonic numerical methods for multi-dimensional compressible flows Part Π: Multi-dimensional limiting process. Journal of Computational Physics, 2005, 208: 570-615.
[30] Kang H M, Kim K H, Lee D H. A new approach of a limiting process for multi-dimensional flow. Journal of Computational Physics, 2010, 229: 7102-7128.
[31] Park J S, Yoon S H, Kim C. Multi-dimensional limiting process for hyperbolic conservation laws on unstructured grids. Journal of Computational Physics, 2010, 229: 788-812.
[32] Park J S, Kim C. High-order multi-dimensional limiting strategy for discontinuous Galerkin methods in compressible inviscid and viscous flows. Computers & Fluids, 2014, 96: 377-396.
[33] Li W A, Ren Y X. The multi-dimensional limiters for discontinuous Galerkin method on unstructured grids. Computers & Fluids, 2014, 96(13): 368-376.
[34] Jawahar P, Kamath H. A high-resolution procedure for Euler and Navier-Stokes computations on unstructured grids. Journal of Computational Physics, 2000, 164(1): 165-203.
[35] Yoon T H, Asce F, Kang S K. Finite volume model for two-dimensional shallow water flows on unstructured grids. Journal of Hydraulic Engineering, 2004, 130(7): 678-688.
[36] Zhang T S, Shahrouz A. A slope limiting procedure in discontinuous Galerkin finite element method for gas dynamics applications. International Journal of Numerical Analysis and Modeling, 2005, 2: 163-178.
[37] Cueto-Felgueroso L, Colominas I, Fe J, et al. High-order finite volume schemes on unstructured grids using moving least-squares reconstruction. Application to shallow water dynamics. International Journal for Numerical Methods in Engineering, 2006, 65(3): 295-331.
[38] Choi H, Liu J G. The reconstruction of upwind fluxes for conservation laws: its behavior in dynamic and steady state calculation. Journal of Computational Physics, 1998, 144: 237-256.
[39] Li W A, Ren Y X. The multi-dimensional limiters for solving hyperbolic conservation laws on unstructured grids. Journal of Computational Physics, 2011, 230: 7775-7795.
[40] Li W A, Ren Y X. The multidimensional limiters for solving hyperbolic conservation laws on unstructured grids Π: Extension to high order finite volume schemes. Journal of Computational Physics. 2012, 231: 4053-4077.
[41] Liu Y L, Zhang W W. Accuracy preserving limiter for the high-order finite volume method on unstructured grids. Computers & Fluids, 2017, 149: 88-99.
[42] Roe P L. Approximate Riemann solvers, parameter vectors, and difference schemes. Journal of Computational Physics, 1981, 43: 357-372.
[43] Jameson A. The Evolution of Computational Methods in Aerodynamics. Journal of Applied Mechanics, 1983, 50(4):1052-1070.
[44] AGARD AR-211, Test Cases for Inviscid Flow Field, AGARD, 1985.
[45] Vassberg C, Jameson A. In pursuit of grid convergence, Part I: Two-dimensional Euler solutions. AIAA paper 2009-4114, 2009.
[46] Woodward P, Colella P. The numerical simulation of two-dimensional fluid flow with strong shocks. Journal of Computational Physics, 1984, 54(1): 115-173.

https://doi.org/10.4208/cicp.OA-2017-0039 Published online by Cambridge University Press